

Buoyant radio plasma in clusters of galaxies 1

2000

Buoyant radio plasma in clusters of galaxies

M. Brüggen^{1,2}, C.R. Kaiser^{1,3}

¹ *Max-Planck-Institut für Astrophysik, Karl-Schwarzschild-Str.1, 85740 Garching, Germany*

² *Churchill College, Storey's Way, Cambridge, CB3 0DS, UK*

³ *current address: Department of Physics & Astronomy, University of Southampton, University Road, Southampton SO17 1BJ, UK*

4 October 2000

ABSTRACT

Radio galaxies are known to inflate lobes of hot relativistic plasmas into the intergalactic medium. Here we present hydrodynamical and magnetohydrodynamical simulations of these hot plasma bubbles in FR II objects. We focus on the later stages of their evolution after the jet has died down and after the bow shock that surrounded the lobes at earlier stages has vanished. We investigate the evolution of the plasma bubbles as they become subject to Rayleigh-Taylor instabilities. From our simulations we calculate the radio and X-ray emissivities of the bubbles and discuss their appearance in observations. Finally, we investigate the influence of large-scale magnetic fields on the evolution of the bubbles. The issues of re-acceleration and diffusion of relativistic particles are briefly discussed.

Key words: radio galaxies, jets, hydrodynamics: MHD

1 INTRODUCTION

The jets of radio galaxies and radio-loud quasars are known to inflate large lobes of radio plasma in the Inter Galactic Medium (IGM). These regions appear either as well-defined cavities in the case of Fanaroff - Riley (FR) type II objects (Fanaroff & Riley 1974) or form broad, more diffuse outflows in FRI objects. In this paper we concentrate on the evolution of the radio lobes of the more powerful FR II objects. In our view, the dynamics of FRIs are more complex and we will refer a discussion of these to a future paper.

The standard model for FRIIs explains the lobes as overpressured bubbles that expand supersonically into the surrounding intergalactic medium (IGM) (Scheuer 1974). In principle, the lobes are unstable because they are surrounded by the denser, unperturbed IGM in the gravitational potential well of the host galaxy. This situation should cause the buoyant lobes to rise through the ambient medium (e.g. Gull & Northover 1973). However, as long as the bow shock, caused by their supersonic expansion, protects the radio lobes, buoyant forces are not important for the dynamics of the lobes (Scheuer 1974). Analyses of spectral ageing show that the jet phase may last for a few 10^8 years (e.g. Alexander & Leahy 1987) after which the jets presumably stop supplying energy to the lobes. After that, they may still be overpressured with respect to the IGM and continue to expand, driving a bow shock. This phase resembles that of a strong explosion or supernova remnant (e.g. Sedov 1959).

The continued expansion of the lobes will bring them

into pressure equilibrium with the IGM. At this point, the bow shock vanishes and the lobes become susceptible to Rayleigh-Taylor instabilities. Because of the absence of strong surface tension in the radio lobes, this situation is reminiscent of the later phases of strong (nuclear) explosions in the Earth's atmosphere. In both cases, the hot rarefied gas forms a torus which, in its wake, drags material up into the atmosphere. Thus the bubble develops a shape that resembles a mushroom. This was discussed in connection with the large scale radio structure of M87 by Böhringer et al. (1995), Churazov et al. (2000a) and Churazov et al. (2000b).

In this paper we extend the hydrodynamical simulations for the specific case of M87 presented in Churazov et al. (2000b) to more general initial configurations. Moreover, we performed MHD simulations to study the influence of a magnetic field that is initially aligned with the physical boundary of the radio lobes. We also present predictions for the radio synchrotron emission from the magnetised plasma within the lobes. Finally, we demonstrate that neither re-acceleration processes nor inhomogeneous magnetic fields in the radio lobes significantly alter the emission properties of the lobes unless the diffusion of particles from weak fields to high field regions is slow.

The paper is organised as follows: We discuss our methods and assumptions in Sec. 2. The results of the simulations are presented in Sec. 3, their observational consequences in Sec. 4 and the conclusions in Sec. 5.

2 METHOD

2.1 Magneto-hydrodynamical simulations

The simulations were obtained using the ZEUS-3D code which was developed especially for problems in astrophysical hydrodynamics (Stone & Norman 1992a, b). The code uses finite differencing on a Eulerian or pseudo-Lagrangian grid and is fully explicit in time. It is based on an operator-split scheme with piecewise linear functions for the fundamental variables. The fluid is advected through a mesh using the upwind, monotonic interpolation scheme of van Leer. The magnetic field is evolved using a modified constrained transport technique which ensures that the field remains divergence-free to machine precision. The electromotive forces are computed via upwind differencing along Alfvén characteristics. For a detailed description of the algorithms and their numerical implementation see Stone & Norman (1992a, b).

As initial model we employed an isothermal model, where the density is given by the β -model, i.e.

$$\rho(r) = \frac{\rho_0}{[1 + (r/a_0)^2]^{3\beta/2}}. \quad (1)$$

We assumed $\beta = 0.5$, $\rho_0 = 1.6 \cdot 10^{-27} \text{ g cm}^{-3}$ and a core radius of $a_0 = 200 \text{ kpc}$, which are typical values for clusters of galaxies (e.g. Jones & Forman 1984). From this, the gravitational potential was calculated such as to keep the background density in hydrostatic equilibrium. The gravitational potential remained fixed during the simulation, which saved us solving Poisson's equation as part of the simulation. We chose dimensionless units, which are defined by $a_0 = 1$, $\rho_0 = 1$ and a gravitational constant of $G = 1$. In our simulations we employed an ideal gas equation of state and we ignored the effects of rotation and radiative processes.

The simulations were performed in 2D on a spherical grid (r, θ) with 200×200 grid points. The grid span 1 Mpc in the radial direction (400 kpc for model D - see below) and π rad in the angular direction.

At the centre, a hot bubble of various geometrical shapes (see below) was set up. It was made buoyant by lowering its density with respect to the background density by a factor of 100 and simultaneously raising the temperature by the same factor. Thus the bubble is in pressure equilibrium with its surroundings. The gas is treated as a single fluid and is assumed to obey a polytropic equation of state with $\gamma = 5/3$. The bubble was filled with 3000 tracer particles that are advected with the fluid.

The low frequency radio lobes of active FR II-type radio sources have elliptical shapes similar to cigars (e.g. Blundell, Kassim & Perley 2000). We also chose elliptical shapes for the initial configurations of our buoyant bubbles. Moreover, it is observed that some radio lobes are “pinched”: The weakening of the bow shock towards the end of the overpressured phase is not an instantaneous process. The sideways expansion of the lobes proceeds more slowly than the expansion in the direction of the jet. Moreover, the regions of the lobe closest to the jet are located in the regions of highest pressure. Therefore, it is likely that the bow shock will start to weaken towards the centre of the radio source leading to a pinched appearance (e.g. Baldwin 1982). We address the effect of such a pre-pinch in one of our models.

In our purely hydrodynamical simulations, we assume that the magnetic field is tangled on scales much smaller than the numerical resolution and that, consequently, it only plays a passive role in our simulations. It has been suggested that the magnetic field may be compressed at the edges of the radio lobes of active FR IIs. This may lead to a more ordered field configuration with the field lines preferentially aligned along the lobe surface (Laing 1980 and references therein). We used the MHD capabilities of ZEUS-3D to investigate such configurations.

In total we simulated six different bubble configurations:

- *Model A*: Spherical bubble with a radius of 200 kpc equivalent to the core radius, a_0 .
- *Model B*: Elliptical bubble with its major axis oriented along the external density gradient. The major axis has a length of 400 kpc and the aspect ratio of the ellipse is 4.
- *Model C*: ‘Pinched’ elliptical bubble, whose surface is described by $r = 60 \text{ kpc} / (1 + 0.8 \cos(\theta + \pi))$.
- *Model D*: Small elliptical bubble with a major axis of 100 kpc and an aspect ratio of 4. Note that the major axis of this bubble only extends to half the core radius a_0 .
- *Model Bm1*: Like Model B but with a large-scale magnetic field which is roughly aligned with the bubble surface and which is at the same time divergence-free. The field configuration is shown in Fig. 6 Energy density of the magnetic field corresponds to about 10% of the gas pressure.
- *Model Bm2*: Like Model Bm1 but with a stronger magnetic field of energy density equivalent to 30% of the gas pressure.

2.2 Radio emission from the simulated bubbles

At the start of our simulations, the radio lobes are at least partly filled with relativistic, magnetised plasma. This material will emit synchrotron radiation. The simulations assume a single, non-relativistic fluid throughout the computational grid. In order to approximate the evolution of the relativistic plasma, we need to make the following assumptions (see also Churazov et al. 2000b):

- In Models A through D we assume that the magnetic field within the rarefied bubbles is tangled on small scales. This allows us to treat the field together with the relativistic particles as a ‘relativistic fluid’ with an adiabatic index of $\Gamma = 4/3$. The relativistic fluid is confined to small patches intermixed with the thermal fluid. This implies that the two components of the bubbles are mixed macroscopically but not on microscopic scales. In other words, the magnetic field can provide a kind of surface tension on its tangling scale.
- The patches of relativistic fluid are in pressure equilibrium with the thermal fluid. Thus they expand and contract adiabatically but do not influence the overall dynamics of the fluid flow.
- The relativistic plasma and the magnetic field are contained in the rarefied, buoyant bubble. The thermal

pressure acting on the relativistic plasma is balanced by the sum of the energy density of the tangled magnetic field, u_B , and that of the relativistic particles, u_e . Initially, we assume a power law for the energy distribution of the relativistic particles with a high-energy cut-off at γ_{\max} . In terms of the particle Lorentz factor, this can be written as $n_e d\gamma = n_o \gamma^{-p} d\gamma$, where we assumed $p = 2$ and $\gamma_{\max} = 10^6$. At the start of the simulations we choose a value for the energy density of the magnetic field, u_B , which is uniform throughout the bubble. The normalisation constant, n_o , is then fixed by the requirement of pressure equilibrium with the thermal fluid.

For models Bm1 and Bm2 the magnetic field is evolved explicitly by the MHD module of the ZEUS code. In these models we make the same assumptions as in the other models except those for the magnetic field.

Adiabatic expansion, synchrotron radiation and inverse Compton scattering of the Cosmic Microwave Background (CMB) radiation lead to changes of the energy distribution of the relativistic particles. The first two processes depend on the local conditions of the relativistic plasma. Furthermore, all energy losses are cumulative. In order to determine the energy distribution of the relativistic particles at a particular time at a given point in the simulation, we need to know its entire ‘loss history’. This is achieved by tracking the conditions at the position of the tracer particles which are advected with the fluid flow. Assuming pressure equilibrium and adiabatic behaviour of the relativistic fluid, we can thus calculate the energy density of the magnetic field, $u_B(t) = u_B(t_o)[p_{th}(t)/p_{th}(t_o)]$, and the normalisation of the particle energy spectrum, $n_o(t) = n_o(t_o)[p_{th}(t)/p_{th}(t_o)]^{3/4}$. The latter is only correct if the diffusion of relativistic particles can be neglected. Using this equation and interpolating linearly between computational time steps, the energy distribution of the relativistic particles can be constructed iteratively (e.g. Kaiser, Dennett-Thorpe & Alexander 1997). Together with the local energy density of the magnetic field, it is straightforward to calculate the synchrotron emissivity at any given position of a tracer particle (e.g. Longair 1991). In all simulations with elliptical bubbles the initial symmetry axis along the major axis of the ellipse is preserved at later times. Assuming rotational symmetry about this axis, we can obtain a 3-dimensional model of the synchrotron emissivity of the flow. Surface brightness maps are computed by line of sight integration assuming optical thin conditions.

3 RESULTS OF THE SIMULATIONS

3.1 The role of asymmetry

Fig. 1 shows the results of our simulation for Model A: a spherical bubble in the centre of the external density profile. We did not perturb the bubble surface but only destroyed the symmetry by raising the density of a single cell by a few percent. Thus the configuration is very symmetric and stable. The high degree of symmetry of the initial configuration prevents any large-scale motions. Rayleigh-Taylor

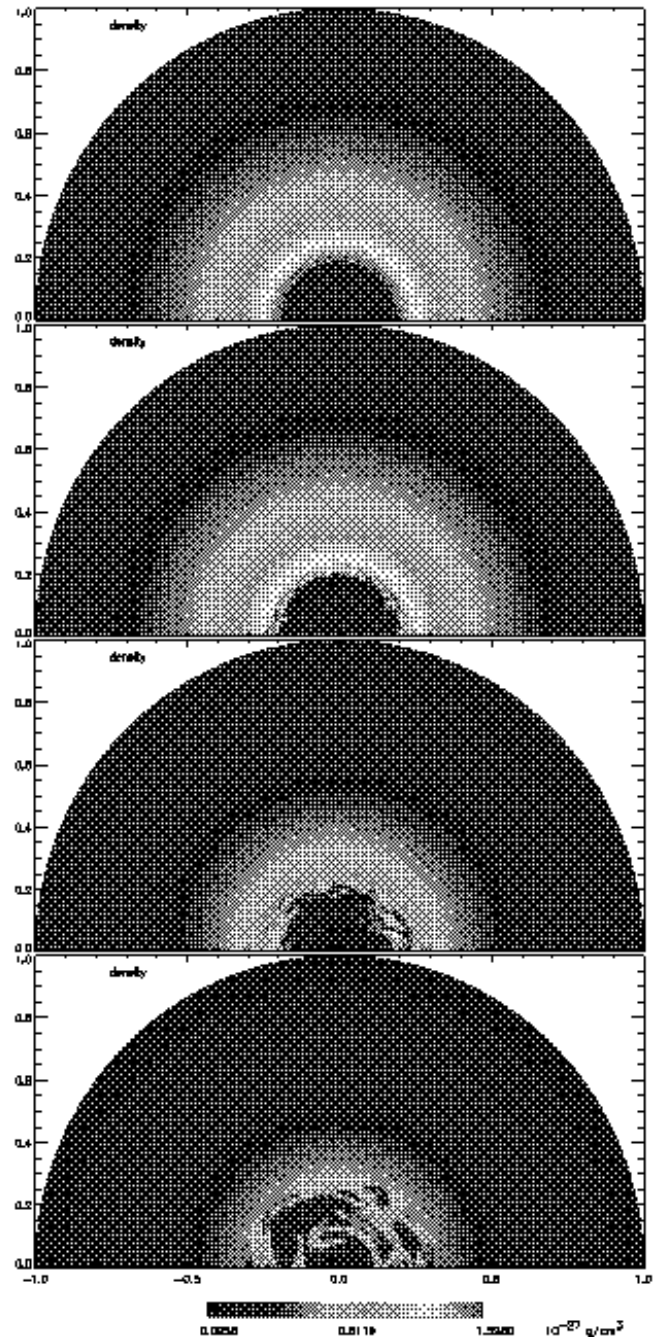


Figure 1. Density maps of a spherical bubble (Model A, see text) at four time steps. From top to bottom: Initial configuration, after 1.86 Gyrs, after 2.23 Gyrs and after 2.60 Gyrs. In this and all other figures, except Fig. 4, unity on axes corresponds to 1 Mpc.

instabilities only start growing after about 1.8 Gyrs. The instability begins on small scales with the occurrence of small ‘mushrooms’ which develop at the density interface. These mushrooms are characteristic for the Rayleigh-Taylor instability and are also seen in laboratory experiments. The small instabilities grow and eventually lead to macroscopic mixing of the bubble material with the ambient medium after another 400 Myrs. The growth of the instabilities is consistent with theoretical predictions: Neglecting the effects of compressibility, the growth rate, Γ , for an instability with a characteristic wavelength λ is approximately $\Gamma^2 \sim g(\rho_a - \rho_b)/\lambda(\rho_a + \rho_b)$, where g is the gravitational acceleration, and ρ_a , ρ_b are the mass densities of the ambient and the bubble gas densities, respectively (e.g. Chandrasekhar 1961).

In Fig. 2 we show the results for Model B. Due to its elliptical shape this model is less symmetric than the spherical bubble of model A. This leads to a faster growth of surface instabilities on large scales. The largest perturbation that pinches off parts of the bubble is already well developed after about 45 Myrs. Small-scale instabilities are visible along the edge of the bubble at this time but they are far less significant than the pinch. After 100 Myrs the mushroom shape is fully formed, leaving some bubble material behind at the centre of the gravitational potential. The mushroom cap evolves further into a torus with some denser ambient gas being entrained in the torus centre. Denser material surrounding the ‘trunk’ of the mushroom is lifted up in the wake of the ascending bubble. Finally, after about 300 Myrs instabilities along the outer surface of the primary torus lead to a split of the torus.

Several sound waves propagate through the ambient gas. The most notable of these is a compression wave which at early times envelopes the top part of the bubble. More sound waves are visible at other stages of the simulation but they are rather weak compared to the primary wave.

In Sec. 2.1 we discussed the possibility that a pinch at the centre of the otherwise elliptical radio lobes may occur before the start of the buoyant phase simulated here. In model C we simulated the effect of such a pinch at the centre of the radio lobe (see top panel of Fig. 3). The major axis of the bubble in model C is shorter than that of model B. Nevertheless, as can be seen by comparing Fig. 2 and 3, the evolution of the bubble is remarkably similar in the two models. The existence of an already pinched shape does not significantly accelerate the growth of the pinching instability. The bubble in model C seems to pinch off at a somewhat lower position along the lobe than that of model B. After the formation of the mushroom at around 200 Myrs, models B and C only differ in the sizes of their bubbles which is mainly due to their different initial sizes.

All the radio lobes shown so far extend to twice the core radius of the external density profile, a_0 . The acceleration, g , due to the underlying gravitational potential rises linearly for distances small compared to a_0 and falls off as $1/r$ at large distances r . The acceleration reaches its maximum at $r = a_0$ and so all models presented here, except for model D, simulate bubbles which initially experience the maximum gravitational acceleration about halfway along their lengths.

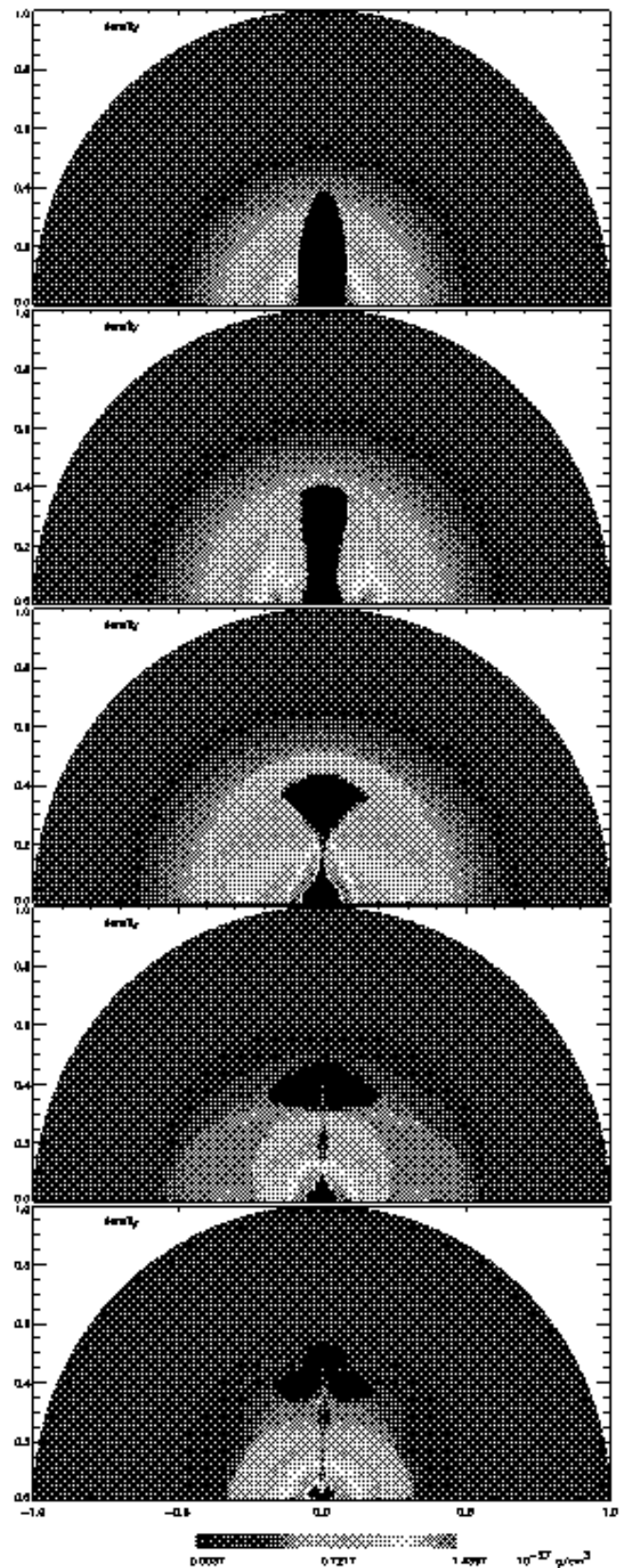


Figure 2. Density maps of an elliptical bubble (Model B, see text) at five time steps. From top to bottom: Initial configuration, after 46.5 Myrs, after 108.5 Myrs, after 217 Myrs and after 310 Myrs.

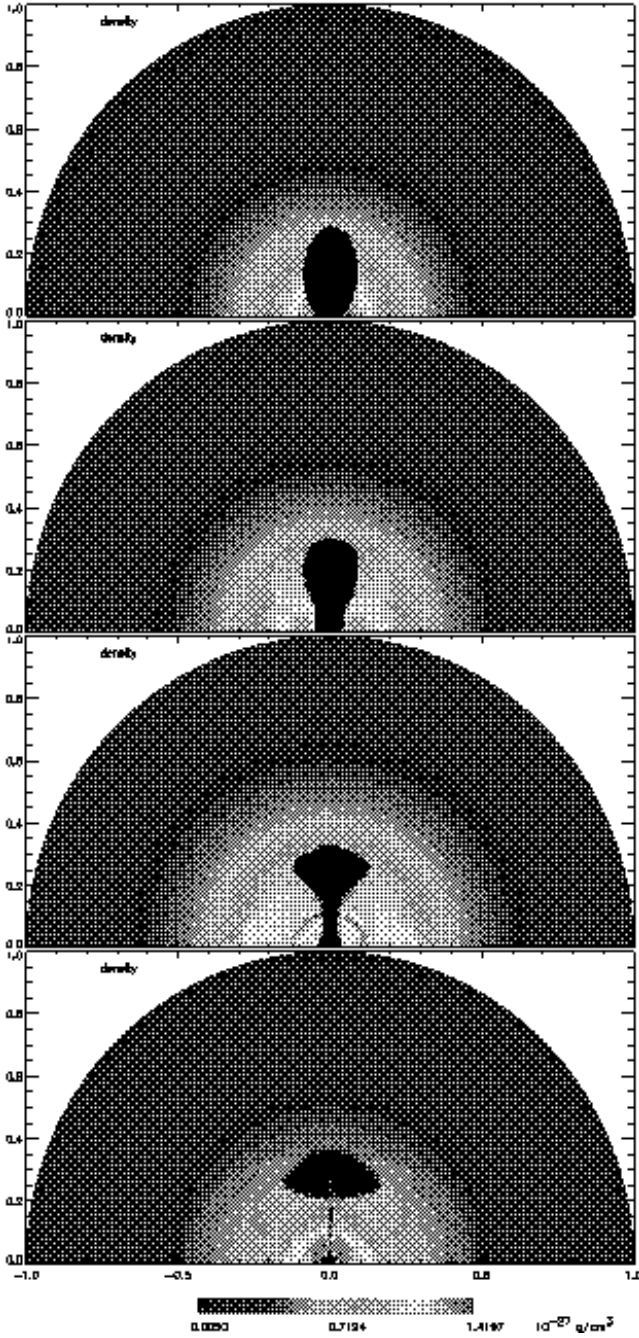


Figure 3. Density maps of a ‘pre-pinch’ elliptical bubble (Model C, see text) at four time steps corresponding to the first four panels of Figure 2. From top to bottom: Initial configuration, after 46.5 Myrs, after 108.5 Myrs and after 217 Myrs.

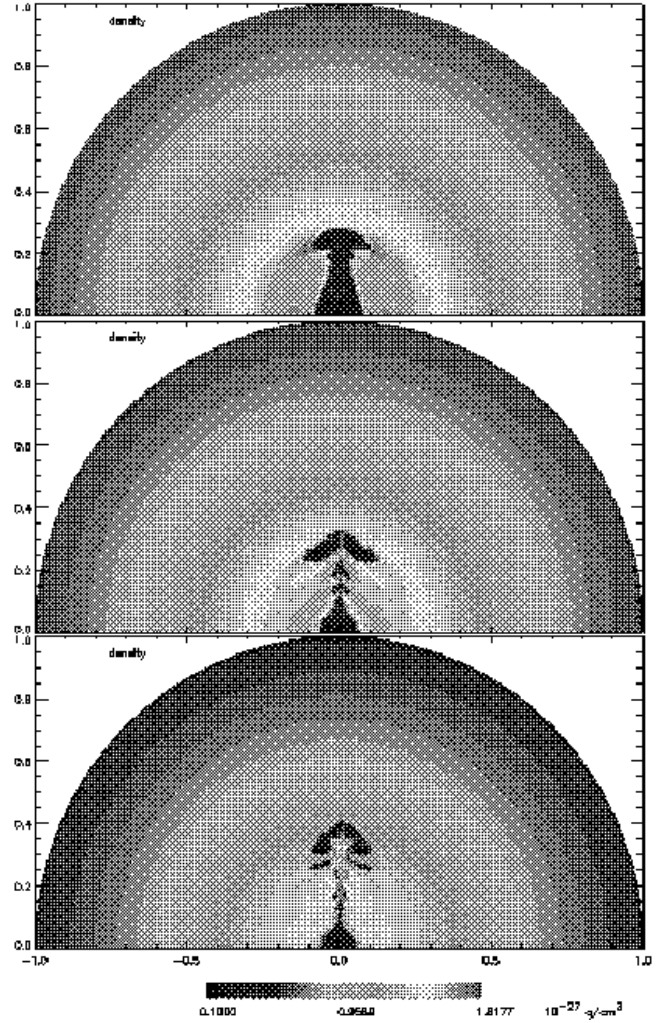


Figure 4. Density maps of an elliptical bubble inside the core radius (Model D, see text) at three time steps corresponding to the last three panels of Fig. 2. From top to bottom: After 124 Myrs, after 217 Myrs and after 310 Myrs. In this figure unity on the axes corresponds to 400 kpc.

Also, for most of their evolution the front ends of the bubbles are immersed in a density profile roughly following a power law distribution outside the core radius. In model D the bubble only extends to half the core radius. Since the bubble is located inside the core radius, the density profile of the surrounding medium does not approximate a power law. Fig. 4 shows the results for this model. Note that this figure shows only the inner 400 kpc of the cluster gas while all other figures extend to 1 Mpc. The initial configuration is not shown as it is similar to a scaled version of the first panel of Fig. 2. The bubble also develops a mushroom shape but this happens slightly later than for the larger bubbles. The pinching instability occurs further out and secondary pinches develop along the rather thick trunk of the developing mushroom. At the end of the simulation at least five separate tori are discernible. The uplifted denser material is clearly visible in the centre of the torus.

The simulations presented here extend the simulations performed by Churazov et al. (2000b). They employed a

background density profile that was derived from observations of the cluster around Virgo A. Within this model they set up a spherical, buoyant bubble which was off-set from the cluster centre. Again a rising torus develops which splits into two tori at later times but no ‘trunk’ is observed. These results demonstrate how sensitive the detailed morphology of the buoyant bubbles depends on the initial conditions. Nevertheless, the development of a rising torus which lifts up ambient material from the centre is generic.

Finally, we should briefly discuss the accuracy of these kinds of finite-difference hydrodynamical simulations. While the code can simulate large-scale mixing due to Rayleigh-Taylor and Kelvin-Helmholtz instabilities, it does not include real diffusion of particles. Any observed diffusion is therefore entirely numerical. Any sharp density discontinuities becomes less sharp as they are advected across the grid due to discretization errors in the advection scheme. For a test of the advection algorithm in the ZEUS code see Stone & Norman (1992). Therefore, the small features in our simulation are likely to be affected by these advection errors whereas the larger features are not.

Second, numerical viscosity is also responsible for suppressing small-scale instabilities at the interface between the buoyant bubble and the surrounding gas. To assess the effects of numerical viscosity, we have repeated our simulations on grids with 100×100 grid points. From our experiments we can conclude that “global parameters” such as the position and size of the bubble as well as the presence of “toroidal” structure are relatively insensitive to the resolution. The detailed developments of the morphology on small scales do depend on the resolution and the initial conditions.

3.2 Rise velocity

The simplest velocity estimate of the rising bubble can be obtained by equating the ram pressure and buoyancy forces acting upon a bubble (e.g. Gull and Northover 1973). The buoyancy force is obviously:

$$F_b = Vg(\rho_a - \rho_b), \quad (2)$$

where V is the bubble volume, g is the gravitational acceleration, ρ_a and ρ_b are the mass densities of the ambient and the bubble gas densities respectively. The drag force is approximately given by

$$F_d \sim C \frac{1}{2} S v^2 \rho_a, \quad (3)$$

where S is the cross section of the bubble. The numerical coefficient C (drag coefficient) depends on the shape of the bubble and the Reynolds number. For a solid sphere moving through an incompressible fluid this coefficient is of the order 0.4–0.5 for Reynolds numbers in the range $\sim 10^3$ – 10^5 (e.g. Landau and Lifshitz 1963). Thus the terminal velocity of the bubble is

$$v \sim \sqrt{g \frac{V}{S} \frac{2}{C} \frac{\rho_a - \rho_b}{\rho_a}} \sim \sqrt{g \frac{V}{S} \frac{2}{C}}. \quad (4)$$

Here the factor of $(\rho_a - \rho_b)/\rho_a$ can be dropped if the

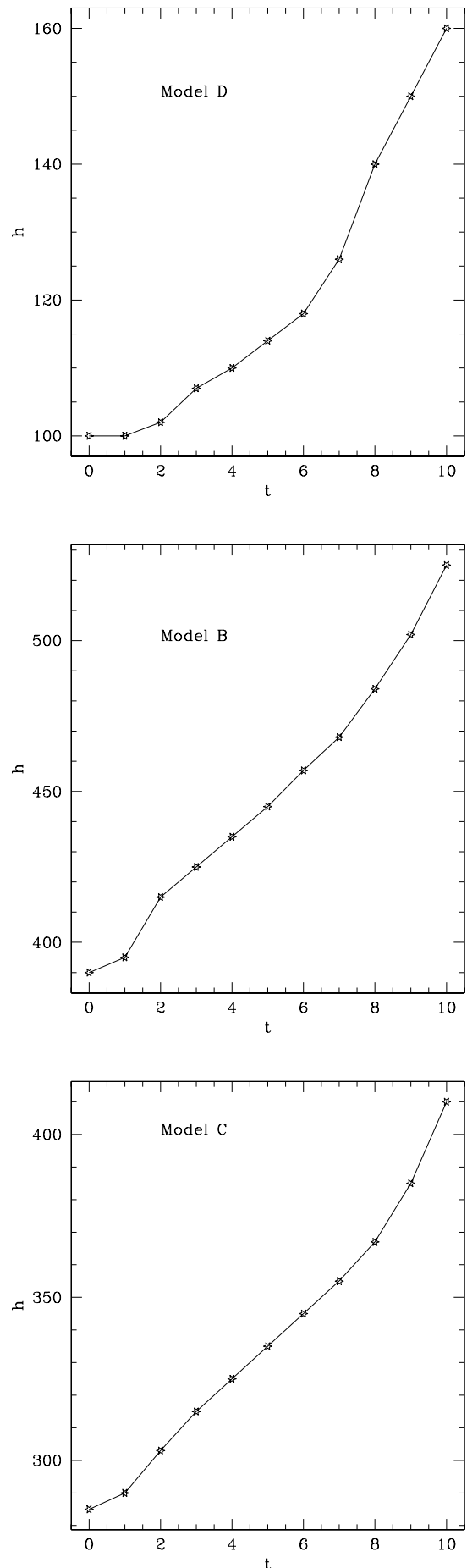


Figure 5. Position of the bubble front as a function of time for models B, C and D.

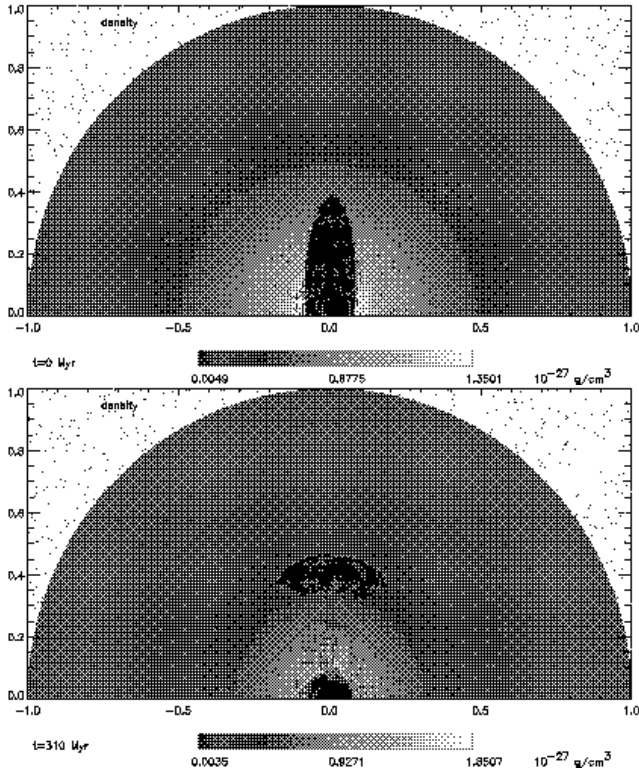


Figure 6. Density map of an elliptical bubble with a ‘weak’ magnetic field aligned with the bubble surface (Model Bm1, see text) at the start of the simulation and after 310 Myrs. This corresponds to the last panel of Fig. 2. The arrows indicate the strength and direction of the magnetic field.

bubble density is low compared to the ambient gas density. The expression for the terminal velocity can be further rewritten using the Keplerian velocity at a given distance from the cluster center: $v \sim \sqrt{(r/R)(8/3C)}v_K$, where r is the bubble radius, R is the distance from the center and $v_K = \sqrt{gR}$ is the Keplerian velocity. Of course the above formula can be used only for order of magnitude estimates of the bubble velocity. Fig. 5 shows the position of the bubble front as a function of time

3.3 Ordered magnetic fields

Fig. 6 shows the final result for model Bm1. This model is identical to model B shown in Fig. 2 except that we added a magnetic field that is initially aligned with the bubble surface. The energy density of the magnetic field corresponds to about 10% of that of the thermal gas. The evolution of the bubble is very similar to that in model B. The only slight difference is that a larger bubble is left behind at the centre of the gravitational potential in model Bm1. The magnetic field is not strong enough to prevent the pinching instability and the bubble forms a mushroom as before. However, the field is able to suppress the break-up of the rising torus during the late stages of the simulation. The magnetic field is still aligned with the surface of the torus (see Fig. 6) and stabilises it against Rayleigh-Taylor and Kelvin-Helmholtz instabilities.

If the magnetic field, initially aligned with the bubble

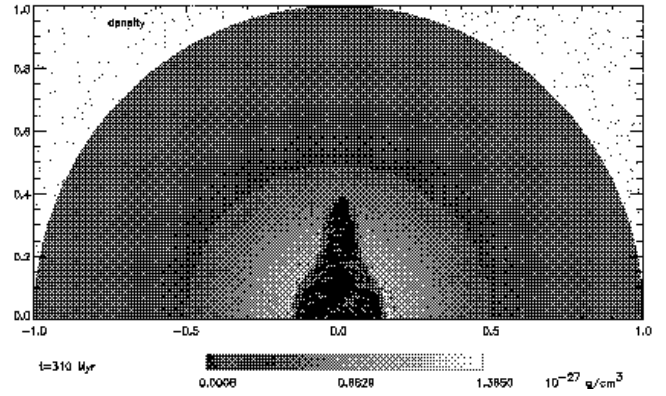


Figure 7. Density map of an elliptical bubble with a strong magnetic field aligned with the bubble surface (Model Bm2, see text) at 310 Myrs after the start of the simulation. This corresponds to the last panel of Fig. 2.

surface, is stronger, it can provide enough surface tension to prevent the pinching instability. Model Bm2 is identical to Bm1 but the energy density of the magnetic field is by about a factor 3 higher. Fig. 7 shows the final stage of this simulation. The magnetic field prevents the development of a pinch and the configuration shown is essentially stationary. The circular shape of the lower part of the bubble results from an expansion in this region driven by the additional pressure exerted by the magnetic field. This configuration resembles the spherical bubble of Model A but in model Bm2 the magnetic field suppresses the small scale instabilities on the surface. We conclude that the magnetic field can stabilise the bubble against Rayleigh-Taylor instabilities. However, this requires a very ordered field structure and a field strength which corresponds to a significant fraction of the thermal pressure. It is unlikely that this configuration is present in real radio lobes.

4 DETECTION OF BUOYANT BUBBLES

It seems very likely that at the end of the lifetime of their jets many powerful radio sources give rise to the buoyant structures in clusters. Here we investigate whether they are directly observable.

4.1 X-ray signature

In our simulations we lowered the density of the bubble material by a factor of 100 with respect to the density of the ambient gas. This implies that in regions filled with bubble material the X-ray surface emissivity is strongly reduced (see Churazov et al. 2000b). Zhidov (1977) showed that even in the presence of surface tension small-scale surface instabilities may lead to a fast break-up of the initial volume into smaller bubbles. Because of the finite resolution of our simulations, we can not exclude that microscopic mixing is efficient. However, the overall geometry of the buoyant bubble, i.e. the development of a mushroom shape, is not affected by this small-scale mixing. This implies that the decrement in the X-ray emissivity within the buoyant bubbles may be

much weaker than is suggested by our simulations. Nevertheless, the dense material uplifted by the rising torus from the centre of the external density distribution will enhance the X-ray emissivity in the wake of the torus (Churazov et al. 2000b). This may be identified in some clusters with observed X-ray features extending radially from the cluster centres (e.g., Böhringer 1995, Churazov et al. 2000b).

4.2 Radio synchrotron emission

Using the assumptions summarised in Sec. 2.2, we calculated maps of the radio surface brightness of the buoyant bubbles due to synchrotron radiation. In addition, we assumed an Einstein-de Sitter universe with $H_0 = 50 \text{ km s}^{-1} \text{ Mpc}^{-1}$ and a redshift of the simulated cluster of $z = 0.1$. Except for the models that include a large-scale magnetic field, Bm1 and Bm2, we are free to choose the strength of the initial field. We considered two cases: A low field with $B_{\text{initial}} = B_{\text{CMB}}/\sqrt{3} = 2.3 \mu\text{G}$, where B_{CMB} is the equivalent magnetic field strength of the CMB, and the equipartition case. In both cases the sum of the partial pressures of the magnetic field and that of the relativistic particles balances the local thermal pressure. The low magnetic field was chosen because it allows for the maximum life time of the relativistic particles (e.g. Churazov et al. 2000a).

Fig. 8 shows the result for the low field case and an observing frequency of 330 MHz. In these maps the major axis of the ellipse is in the plane of the sky. Even after $2 \cdot 10^8$ years the bubble is clearly detectable. The bubble appears to be broadened compared to the density plots in Fig. 2 because of the lower numerical resolution provided by the advected tracer particles compared to the computational grid.

Fig. 9 shows the same model as 8 but with the assumption that the magnetic field pressure and the thermal pressure are in equipartition. In this case, the initial magnetic field is stronger, $B \sim 15 \mu\text{G}$. Consequently, in the early phases the bubble is much brighter than in the low field case; the peak surface brightness in the first panel of Fig. 9 is above 1 Jy/pixel . This increased emission of synchrotron radiation leads to faster energy losses of the relativistic particles and so the bubble dims more rapidly than in the low field case. After roughly $1.5 \cdot 10^8$ years it has faded completely.

The radio surface brightness distributions resulting from the other models considered in previous sections are qualitatively very similar to that of model B. The total radio flux and the spectra depend more on the assumptions for the strength of the magnetic field, the energy distribution of the relativistic particles and the pressure in the environment than on the morphology of the fluid flow. We also found that the models which include large-scale magnetic fields showed little difference in terms of total radio luminosity. Of course, in these cases the magnetic field is very ordered and will give rise to strong polarisation of the synchrotron emission. Rottmann et al. (1996) find polarised emission from the edges of the buoyant large scale structure of M87. This seems to suggest some ordering of the field in this object. However, this may simply reflect the compression of the magnetic field along the leading edge of the rising

torus and is no indication of an initially ordered field.

In our calculations of the synchrotron radio emission we start with a power-law energy distribution for the relativistic particles with a rather high cut-off ($\gamma_{\text{max}} = 10^6$). This initial stage corresponds to the point of pressure equilibrium between the radio lobes and the ambient medium. If the relativistic particles in the lobes of radio sources are only accelerated at the shock at the end of an active jet then there will be no replenishment of these particles once the jet is switched off. As pointed out above, at this stage the lobes may still be overpressured with respect to the ambient medium. The subsequent expansion phase without jet flow may well be comparable or longer than the radiative lifetime of the more energetic electrons. In this case, the high energy cut-off of the distribution will be much lower than we assumed here. The lobes will then be undetectable during their buoyant phase.

Other effects such as *in situ* re-acceleration and diffusion of particles between regions of low and high magnetic field may prolong the radiative lifetime of the bubbles (for the case of M87 see Owen, Eilek & Kassim 2000; Churazov et al. 2000b). If these processes are significant, then no conclusions on the source age can be drawn from the potentially observed position of the break in the radio spectrum. A further problem with these processes is that they require large amounts of ‘hidden’ energy in the relativistic particle population. Radio emission in the GHz-range is emitted by electrons with Lorentz factors of a few thousands. However, in re-acceleration processes usually many more electrons at much lower energies are produced which dominate the total energy density. They have much longer radiative lifetimes than the ‘observable’ electrons. Continued re-acceleration will therefore lead to a build-up of pressure in the relativistic fluid, quickly dispersing the emission region. In the case of an inhomogeneous magnetic field in the lobes, the relativistic particles have to diffuse slowly from regions of low magnetic field to high field regions. If the typical diffusion time is short compared to the radiative lifetime of the particles, then this kind of diffusion does not significantly change the emission properties. In other words, if diffusion is efficient, this case resembles that discussed above where electrons are permanently in the high field region. For inefficient diffusion only a small fraction of the relativistic particle population is observable. The total energy density of the particles in the low field regions, the ‘reservoir’, is limited by the thermal pressure of the surrounding fluid. This implies that, compared to the radio maps shown in Figs. 8 and 9, such a source may radiate for longer but would be very faint.

Another possibility to extend the radiative lifetime of the buoyant lobes is the local amplification of the magnetic field by shear flows or other turbulent processes. These regions of stronger magnetic field may then enable a comparatively unaged population of relativistic particles to ‘light up’. However, even if we neglect adiabatic and synchrotron energy losses altogether, a maximum lifetime of relativistic particles is set by the IC scattering of the CMB. This limits the time for which the radio plasma is observable to roughly $2.3 \cdot 10^9 (1+z)^{-4}$ years. The level of turbulence in the bubble which amplifies the magnetic field is likely to decrease with time. Also the total supply of relativistic electrons is still depleted by consecutive shearing events. Therefore, the

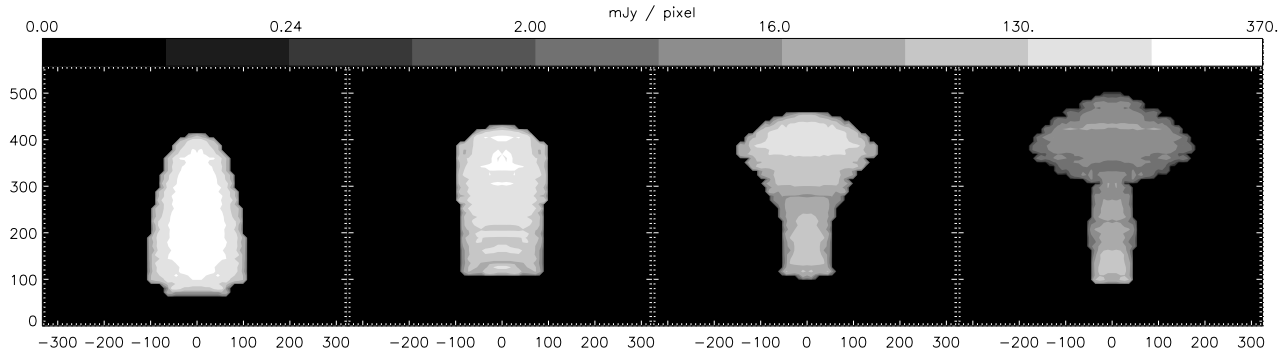


Figure 8. Radio emission from model B assuming an initial magnetic field strength of $2.3 \mu\text{G}$ and pressure equilibrium. The observing frequency is 330 MHz and for the redshift we assume $z = 0.1$. The volume filling factor of the radio plasma is unity. The units along the axes are kpc and the size of an individual pixel is 9×9 kpc or roughly 3.7 arcsec^2 for the chosen redshift. From left to right the panels show the bubbles at start of the simulation, after 46.5 Myrs, after 108.5 Myrs and after 217 Myrs. They correspond to the first four panels of Fig. 2.

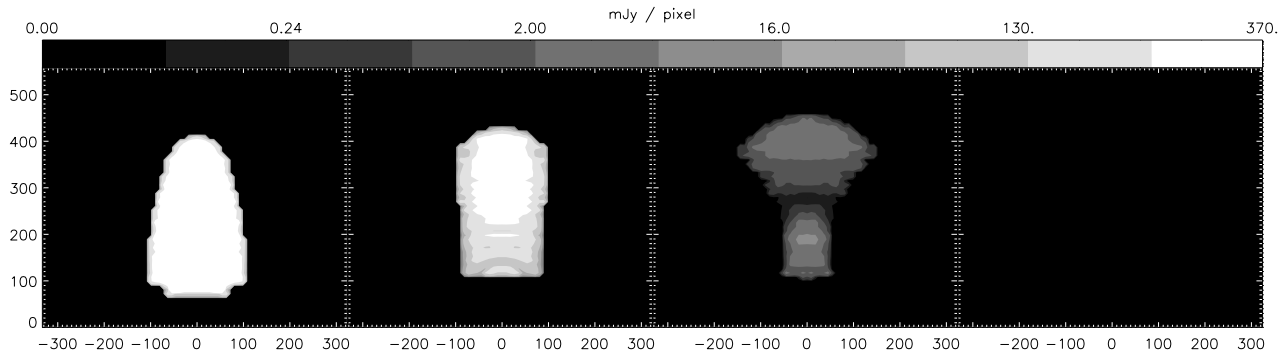


Figure 9. Same as Fig. 8 but assuming equipartition between the magnetic field and the relativistic particles at the start of the simulation.

radio emission again is expected to be faint at later times in this scenario.

5 CONCLUSIONS

Using hydrodynamical simulations, we investigated the evolution of buoyant bubbles of different sizes and geometries in a galactic gravitational potential. Common to all simulations with a non-spherical bubble is the formation of a large mushroom-shaped lobe that rises through the ambient medium. It is interesting to note that the hot plasma remains confined within a single cloud for a considerable time without requiring surface tension or magnetic fields. This is also observed in the evolution of buoyant thermals which are formed, for example, in strong nuclear explosions in the Earth's atmosphere. In their wake the bubbles lift colder material upwards.

Differences between simulations with different initial geometries become manifest in different rise velocities and somewhat different morphologies of the buoyant bubble. We have selected a set of initial conditions to show the ranges of rise velocities and morphologies that can occur. The growth times as well as the morphologies of the instabilities are quite different for spherical and elongated bubbles. Only in the latter case a large ‘mushroom’ forms. This ‘mushroom’

rises upwards as a whole before it succumbs to instabilities on smaller scales. Spherical bubbles, however, evolve very differently: Due to their symmetry, Rayleigh-Taylor instabilities mix the material in the bubble with the ambient fluid *before* any large-scale motions can occur. Our conclusions have to be diluted by the usual caveats that come with finite-difference simulations. Our simulations merely serve as toy models that demonstrate the underlying physics and show the global morphology of the evolving bubbles. The reader should bear in mind that the detailed morphologies on smaller scales depend on the numerical procedure, the resolution of the grid and the details of the initial model. Moreover, we only presented 2D simulations which may produce artificial features. However, we have repeated some of our simulations in 3D on a grid with much smaller resolution and did not find significantly different results.

We also performed MHD simulations where the bubbles were filled with a magnetic field that was parallel to the surface of the bubble. It was found that the magnetic field helps to protect the rising bubbles against secondary Rayleigh-Taylor and Kelvin-Helmholtz instabilities. Only a strong and ordered magnetic field, where the magnetic pressure is comparable to the thermal pressure, may suppress the formation of the mushroom structure.

Finally, we calculated maps of the radio surface bright-

ness due to synchrotron radiation. These maps were compiled for two different assumptions about the magnetic field strength: (i) a low field, where the initial field strength is roughly equal to the equivalent field strength of the CMB, and (ii) a strong field, where the energy density of the magnetic field and that of the relativistic particles are in equipartition. In the weak-field case, the bubble is visible in the radio for more than $2 \cdot 10^8$ years, whereas in the strong-field case the higher energy losses cause the radio image to fade after $1.5 \cdot 10^8$ years. We discuss various processes of re-acceleration and diffusion of relativistic particles as well as their influence on the synchrotron radiation properties of the bubbles. We find that some of these processes may prolong the phase of synchrotron emission but if so, the bubbles will be exceedingly faint at radio frequencies.

Acknowledgements

It is a pleasure to thank Eugene Churazov for helpful discussions.

REFERENCES

- Alexander P., Leahy J. P., 1987, MNRAS, 225, 1
 Baldwin J. E., 1982, in Heeschen D. S., Wade C. M., eds, Extragalactic radio sources. Reidel, p. 21
 Blundell K. M., Kassim N. E., Perley R. A., 2000, in et al. R. D. E., ed, The universe at low radio frequencies. ASP Conference Series, in press.
 Böhringer H., Nulsen P. E. J., Braun R., Fabian A. C., 1995, MNRAS, 274, L67
 Chandrasekhar, S., 1961, *Hydrodynamic and Hydromagnetic Stability*, Clarendon Press, Oxford
 Churazov E., Brügggen M., Kaiser C. R., Böhringer H., Forman W., 2000b, ApJ: submitted.
 Churazov E., Forman W., Jones C., Böhringer H., 2000a, A&A, 356, 788
 Fanaroff B. L., Riley J. M., 1974, MNRAS, 167, 31
 Gull S. F., Northover K. J. E., 1973, Nat., 224, 80
 Jones C., Forman W., 1984, ApJ, 276, 38
 Kaiser C. R., Dennett-Thorpe J., Alexander P., 1997, MNRAS, 292, 723
 Laing R. A., 1980, MNRAS, 193, 439
 Landau, L.D., Lifshitz, E.M., 1963, Fluid mechanics, Pergamon Press
 Longair M. S., 1991, High energy astrophysics. Cambridge University Press
 Owen F. N., Eilek J. A., Kassim N. E., 2000, ApJ: submitted.
 Rottmann H., Mack K., Klein U., Wielebinski R., 1996, A&A, 309, L19
 Scheuer P. A. G., 1974, MNRAS, 166, 513
 Sedov L. I., 1959, Similarity and dimensional methods in mechanics. Academic Press, London
 Stone, J.M., Norman, M.L., 1992a, ApJS, 80, 753
 Stone, J.M., Norman, M.L., 1992b, ApJS, 80, 791
 Zhidov, I.G. Meshkov, E.E. Popov, V.V. Rogachev, V.G. Tolshmyakov A.I. 1977, Zhurnal Prikladnoi Mekhaniki i Tehnicheskoi Fisiki , 3, 75